TRENDS IN SCIENCES 2026; 23(4): 12091
https://doi.org/10.48048/tis.2026.12091 RESEARCH ARTICLE

Effect of pH and Calcination Temperature on the Structural, Optical, Electrical, and Magnetic Properties of Co-Precipitated Iron Oxide Nanomaterials

Buppachat Toboonsung

Faculty of Science and Technology, Nakhon Ratchasima Rajabhat University, Nakhon Ratchasima 30000, Thailand

(Corresponding author's e-mail: buppachat.t@nrru.ac.th)

Received: 28 September 2025, Revised: 9 October 2025, Accepted: 19 October 2025, Published: 30 December 2025

Abstract

Iron oxide nanomaterials were synthesized by co-precipitation, with pH adjusted from 9 to 12, and subsequent calcination carried out between 300 and 900 °C. The as-synthesized samples were characterized for morphology, crystal structure, and functional properties. At pH 11, nearly spherical nanoparticles with uniform size and high crystallinity were obtained, giving the highest saturation magnetization of 121.97 emu/g and a narrow indirect optical band gap of 2.03 eV, beneficial for magnetic hyperthermia and visible-light photocatalysis. Calcination at 500 °C retained the γ-Fe_2O_3 phase and yielded peak electrical conductivity (98.62×10^{-9} $(\Omega\cdot cm)^{-1}$) together with near-superparamagnetic behavior with low coercivity and remanence, making it suitable for spintronics and biomedical applications. In contrast, annealing above 500 °C triggered irreversible conversion to antiferromagnetic α-Fe_2O_3, which sharply reduced magnetization and increased electrical resistivity. Combined structural, optical, and magnetic data indicate that pH 11 with 500 °C provides the most favorable trade-off between defect density, phase stability, and interparticle connectivity. Therefore, this work demonstrates that the dual-parameter control of pH and calcination temperature allows the optimization of structural, optical, electrical, and magnetic properties, enabling the development of multifunctional iron oxide nanomaterials for catalysis, biomedicine, and next-generation electronic devices.

Keywords: Iron oxide, Co-precipitation, Optical property, Energy band gap, Electrical resistance, Electrical conductivity, Magnetic properties, Coercivity, Remanence

Introduction

Nanotechnology has emerged as a forefront of modern science and engineering with the relentless pursuit of materials with custom-designed functionalities [1]. Nanostructured materials have properties physically, chemically, electrically, and magnetically compared to their bulk material, providing many innovations [1]. In this great variety of families, iron oxide nanostructures (IONs) belong to those that will be highly instrumental based on exceptional multifunctionality combined with environmentally friendly characteristics and intrinsic biocompatibility, among others [2]. This large potential already ensures applications going from targeted drug delivery and magnetic resonance imaging (MRI) in biomedicine [3] up to environmental remediation [4], catalysis, or even further into novel, highly dynamic areas such as spintronics and next-generation electronic devices [5,6]. Recent studies further demonstrate the expanding role of iron-based nanomaterials in sustainable and advanced applications. For instance, Gabal *et al*. [7] reported a 1-step green synthesis of iron nanoparticles using green tea extract, highlighting their low cytotoxicity and hemostatic potential for biomedical use. In parallel, Yuennan *et al.* [8] showed that iron-containing systems can effectively tailor dielectric properties for flexible electronics [8] and activate peroxymonosulfate for antibiotic degradation in water treatment [9], underscoring the versatility of Fe^{3+}-based materials in both technological and environmental contexts. Among the polymorphic iron oxide phases, maghemite (γ-Fe_2O_3) is particularly relevant to this work due to its

strong ferrimagnetism, chemical stability, and suitability for biomedical and spintronic applications [10,11]. While magnetite (Fe_3O_4) exhibits high electrical conductivity from mixed-valence states [12], and hematite (α-Fe_2O_3) serves as a stable n-type semiconductor (~2.2 eV) for photocatalysis and sensing [10,13], maghemite, being fully oxidized yet magnetically robust, offers an optimal balance for multifunctional use. Its optical band gap (2.0 - 2.2 eV) enables applications in optoelectronics and photocatalysis [10,13]. Its magnetic response supports roles in data storage and magnetically guided therapy [11,14,15]. Precise control over synthesis is therefore essential to tailor these properties for targeted applications.

Various methods have been developed to tailor the size, morphology, and phase purity of IONs, including thermal decomposition [16], precipitation [17], sol-gel [18], chemical routes [19], radiation-chemical methods [20], and hydrothermal techniques [21]. Of these techniques, the co-precipitation method is particularly attractive due to its simplicity, scalability, and low cost for both the fundamental research and industrial scale applications [17,22]. In this process, 2 synthesis parameters play a crucial role: the pH of the medium reaction and the calcination temperature after synthesis [23]. The pH controls the nucleation kinetics, surface charge (zeta potential), and agglomeration behavior, which in turn define final morphology and defect landscape. At the same time, it has been widely reported that crystallinity phase stability and grain growth, dependent on the band structure of IONs, also determine the magnetic domain configuration [24,25]. These parameters play a crucial role, and this is known in the literature. For instance, Ritik *et al.* [22] emphasized that the effectiveness of nano-structured gel materials for environmental and biomedical applications largely depends on the ability to tailor their physicochemical properties, often by modulating variables such as pH [19]. Similarly, Wu *et al.* [23] highlighted in their comprehensive review that recent progress in magnetic iron oxide nanoparticles has been fundamentally driven by advances in controlled synthesis, surface functionalization strategies, and their integration into biomedical applications. They emphasized that precise control over particle size, morphology, and surface chemistry is essential for unlocking multifunctional performance. However, the systematic elucidation of synthesis parameters to realize simultaneous structural, magnetic, optical, and electrical optimization is still one of the important research gaps. Although many of them have investigated the underlying mechanism underpinning the impact of pH or calcination temperature, respectively [26,27], a combined 2-parameter optimization study that associates their synergistic interplay with an extensive set of attributes, including structural, optical, electrical, and magnetic attributes, has been missing. The works published until now tend to only focus their study on 1 aspect, magnetism [12] or photocatalysis [13], and provide a partial image. In addition, how the altered synthesis of 1 product condition propagates throughout all material properties is not well understood. IONs for completely multifunctional needs, that is, high electrical conductivity combined with superparamagnetism and a specific optical band gap, as an instance. In addition, the credibility of such an extensive analysis relies on the rigorous and uniform characterization. An important reference methodology that shows a supported protocol for the direct 2-probe measurement of electrical resistivity [24], and VSM measurements of the magnetic properties [26]. These studies highlight the necessity for reliable characterization when valid property conclusions are to be drawn.

Therefore, the study is carried out to fill this important void, the role of synergistic interplay of synthesis pH (9 - 12) and calcination temperature (300 - 900 °C). The structure evolution, optical bandgap, electrical conductivity, and magnetic behavior in co-precipitated iron oxide nanomaterials were investigated using SEM, XRD, UV-Vis, fluorescence spectroscopy, VSM, and electrical resistivity measurements for a straightforward structure-property relationship. The purpose of the present work is to optimize dual factors of pH and temperature to achieve the maximum values of magnetoresponses, conductivities, and optical properties. In this context, the results described here introduce a simple, experimentally validated methodology for tuning iron oxide nanomaterials that can guide their targeted use in applications ranging from next-generation integrated spintronic devices to multifunctional biomedical platforms and advanced power-efficient catalytic systems.

Materials and methods

Iron oxide nanomaterials were synthesized using the co-precipitation method, with ferrous sulfate ($FeSO_4$) at 0.3 M as the precursor. The reactions were used with magnetic stirring at 350 rpm for 15 min at room temperature. Subsequently, a 1.0 M sodium hydroxide (NaOH) solution was dropped into the iron oxide solution until the pH values reached 9, 10, 11, and 12. The mixture was then continuously stirred for an additional 50 min to ensure complete precipitation. The precipitate was allowed to settle and washed with DI water until a neutral pH was achieved. The washed precipitation was subjected to a controlled heating process, during which the furnace temperature gradually increased from room temperature to the target annealing temperature of 1 h, followed by continuous annealing at 400 °C for 2 h. To investigate the effect of annealing temperature, iron oxide nanomaterials synthesized at the optimum pH were further annealed at 300, 500, 700, and 900 °C, using the same heating rate and a holding time of 2 h as in the previous step. A 1-factor-at-a-time experimental approach was employed: first, the effect of synthesis pH 9 - 12 was investigated at a fixed calcination temperature of 400 °C. The optimal pH 11 was then selected for further study of calcination temperature at 300 - 900 °C. The morphology of the synthesized iron oxide nanostructures was examined using a scanning electron microscope (SEM, JEOL JSM-7800F). The crystal structure was characterized by X-ray diffraction (XRD, Rigaku Smartlab, Cu-Kα radiation at 40 kV and 40 mA). The chemical composition was analyzed using Raman spectroscopy (SENTERRA, a laser wavelength of 532 nm and a power of 12.5 mW). The optical properties, including light absorption, photoluminescence, and energy band gap measurements, were studied using ultraviolet-visible spectroscopy (GENESYS 10S) and fluorescence spectroscopy (JASGO FP8300). The electrical conductivity of the iron oxide nanomaterials was calculated based on their electrical resistivity, which was obtained from direct 2-probe resistance measurements. (multimeter, UNI-T-UT70B, 0 - 40 MΩ). The electrical resistance (R) test was used on the product of 50 mg, pressed by a hydraulic machine at 2 kN in an area (A) of 1×1 cm^2 and a thickness (L) of the plastic insulator of 1 μm at room temperature [24]. Electrical resistance was measured 5 times for each sample, and the average value was used to calculate electrical resistivity (ρ) and electrical conductivity (σ), respectively. Additionally, the magnetic properties were analyzed using a vibrating sample magnetometer (VSM, 7403, LakeShore, USA) at room temperature [25]. All synthesis and characterization procedures were repeated at least 3 times to ensure experimental reliability.

Results and discussion

pH-driven morphological and structural evolution

The variation in pH significantly altered both morphology and crystal structure, suggesting that the synthesis environment dictates nucleation and growth processes. The as-synthesized iron oxide nanomaterials, obtained by varying the pH of the solution and calcining at 400 °C, were examined by scanning electron microscopy (SEM), as shown in **Figures 1(a) - 1(d)**. It was found that the iron oxide nanomaterials synthesized at pH 9, 10, and 11 exhibited a mixture of spherical and flake-like particles with irregular sizes and average diameters of 103, 71, and 63 nm, respectively. The irregular sizes of flake-shaped and an average diameter of 145 nm of iron oxide nanomaterials were shown at the pH of 12, as shown in **Figure 1(d)**. It was noted that higher pH levels during synthesis can lead to increased particle size and morphological changes in iron oxide nanoparticles. For instance, Naushin *et al.* reported that varying the pH during the synthesis of Fe_2O_3 nanoparticles affects their structure, surface charge, and influences their morphology [26]. Similarly, Sayed and Polshettiwar demonstrated that the pH of the solution plays a crucial role in determining the shape and size of iron oxide nanoparticles, with higher pH levels resulting in larger and more flake-like structures [27].

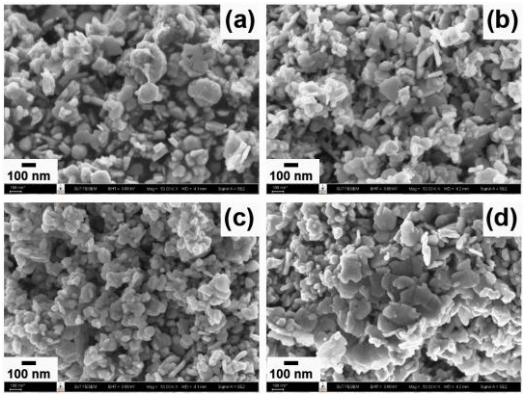

Figure 1 SEM images (50 k× magnification) of iron oxide nanomaterials synthesized at pH values of 9 - 12.

The X-ray diffraction (XRD) patterns of iron oxide nanomaterials synthesized at pH 9 - 12 and annealed at 400 °C were recorded in the range of 20° - 70° as shown in **Figure 2**. The diffraction peaks of Fe_2O_3 corresponded to the planes (210), (211), (220), (311), (222), (400), (422), (511), and (440), indicating a cubic crystal structure consistent with the standard JCPDS No. 39-1346 maghemite (γ-Fe_2O_3). The average crystallite size (D) was determined using Scherrer's equation (Eq. (1)) [7,10,17,24,25].

$$D = K\lambda / \beta\cos\theta \quad (1)$$

where K is a constant taken to be 0.94, λ is the wavelength of x-rays (1.54 Å), β is the full width at half maximum intensity, θ is the Bragg's angle, and D is the crystallite size (nm) [17,21,24,25].

The calculated crystallite size was approximately 24 nm under all pH conditions, indicating that variations in pH did not significantly affect the crystal structure or size of the iron oxide nanomaterials. This observation aligns with reports that the crystallite size of γ-Fe_2O_3 nanoparticles remains relatively constant across different pH levels during synthesis [26]. The SEM results show that the average particle diameter varied significantly with pH (63 - 145 nm). In contrast, Scherrer analysis indicated a nearly constant crystallite size of about 24 nm across all conditions. This suggests that synthesis pH does not strongly influence nucleation but rather governs agglomeration and secondary growth mechanisms, which are affected by the surface charge (zeta potential) of nascent crystallites. At pH 9 - 11, the conditions favored smaller, quasi-spherical agglomerates. In contrast, at pH 12 the sharp transition to larger, flake-like particles indicates a regime dominated by oriented attachment, in which primary crystallites assemble preferentially along specific crystallographic facets. These results confirmed that pH variation 9 - 12 affects only morphology and agglomeration, without altering the crystal phase or primary crystallite size.

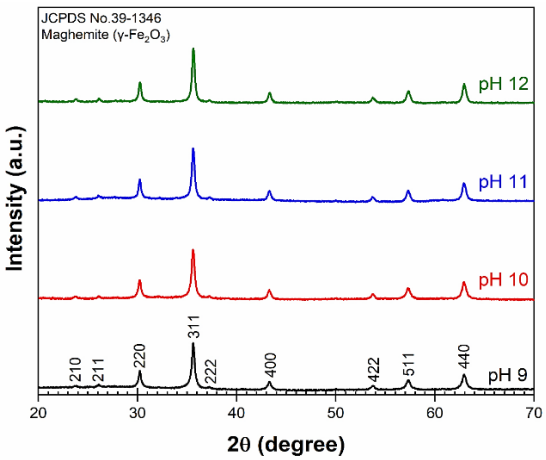

Figure 2 XRD patterns of iron oxide nanomaterials synthesized at pH values of 9 - 12.

Band gap engineering through pH variation

The optical absorption characteristics of the synthesized nanomaterials were probed using UV-Vis spectroscopy (inset, **Figure 3**). All samples exhibit a broad absorption edge spanning 392 - 417 nm, characteristic of iron oxide nanostructures and consistent with prior reports [26]. This absorption arises from electronic transitions from the valence band (primarily O 2p orbitals) to the conduction band (primarily Fe 3d orbitals). To quantitatively determine the optical band gap (Eg), Tauc plot analysis was employed, using the relation for an indirect semiconductor [7,24,25,28-30]:

$$(\alpha h\nu)^2 = A\,(h\nu - Eg) \quad (2)$$

and

$$\alpha = 2.303\,(A_{bs}/t) \quad (3)$$

where α is the absorption coefficient, hν is the photon energy, A is a constant, Eg is the optical band gap, A_{bs} is the absorbance, and t is the effective sample thickness. The band gap was obtained by extrapolating the linear portion of the $(\alpha h\nu)^2$ vs. hν plot to the energy axis (**Figure 3**).

The results reveal a pronounced non-monotonic trend. Samples synthesized at pH 9, 10, and 11 consistently exhibit an optical band gap of 2.03 eV. This stability strongly correlates with XRD data, which showed that the primary crystallite size remained nearly constant at approximately 24 nm across these pH conditions. Such crystallite dimensions are far above the threshold where quantum-confinement effects become significant for iron oxides (typically < 10 nm), indicating that quantum confinement is not the dominant factor controlling Eg in this range [31,32]. However, the optical band gap increases to 2.12 eV at pH 12 was affected by the size of particles, as revealed significantly larger by SEM (flake-like particles, average diameter ≈ 145 nm) at this pH. Conventionally, larger particles would be expected to exhibit a narrower band gap, closer to the bulk value, due to their lower surface-to-volume ratio. The observed widening of the band gap, therefore, requires explanation in terms of defect chemistry and structural order. Defects such as oxygen vacancies (V_O) or interstitial iron atoms (Fe_i) commonly create intra-gap states that reduce the effective optical gap by providing intermediate energy levels for electronic transitions [31-35]. Under the synthesis conditions at pH 12, however, growth appears to favor a more ordered, oriented-attachment-driven assembly of crystallites. The resulting large, well-aligned flakes likely contain fewer grain boundaries and disordered regions, which are typical sites for defect formation. Consequently, a reduction or passivation of defect states would effectively clean up the band structure, shifting the valence and conduction bands farther apart and producing the observed increase in Eg [36]. Prior studies strongly support this interpretation. Adel *et al.* [28] reported that pH during the deposition of Cu_2O thin films directly influenced defect concentrations, which in turn modulated the band gap. Similarly, Choudhury *et al.* [29] showed that oxygen-deficient TiO_2 nanotubes exhibited a narrowed band gap due to defect states, while annealing, which reduces defect density, restored a wider gap. The present findings confirm that pH acts not only as a morphological director but also as an effect on the defect engineering in iron oxide nanomaterials [31-36]. While pH 9 - 11 produced materials with a consistent band gap of 2.03 eV governed by the intrinsic properties of the maghemite phase, Structural reorganization that suppressed defect-mediated gap narrowing, yielding a wider band gap of 2.12 eV induced at pH 12. Therefore, this modest increase may be reduced defect-assisted recombination. This demonstrates that a simple adjustment of synthesis pH can serve as an effective tool for tailoring the optoelectronic properties of iron oxide nanomaterials.

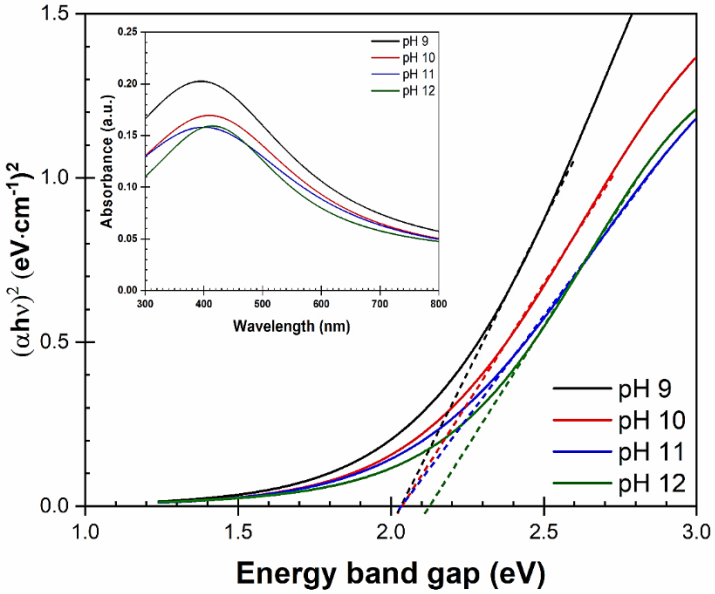

Figure 3 Optical energy band gap values and inset showing the UV-Vis absorption spectra of iron oxide nanomaterials synthesized at pH 9 - 12.

Tuning magnetic performance via pH control

The magnetic response of iron oxide nanomaterials is not fixed but highly tunable, depending sensitively on synthesis conditions. Here, the role of synthesis pH is examined as a critical parameter governing magnetic performance. By systematically varying pH from 9 - 12 while maintaining a calcination temperature of 400 °C, a non-linear dependence of key magnetic parameters, saturation magnetization (Ms), coercivity (Hc), remanence (Mr), squareness ratio (R), and magnetic anisotropy constant (K) is revealed [35,38]. The squareness ratio (R) and the anisotropy constant (K) were calculated by

$$R = Mr/Ms \quad (4)$$

and

$$K = (Hc \times Ms)/0.96 \quad (5)$$

This dependence arises from pH-mediated control over particle size, morphology, and defect structure. Magnetic hysteresis loops obtained from Vibrating Sample Magnetometry (VSM) are shown in **Figure 4**, with quantitative parameters summarized in **Table 1**. All samples exhibit hysteresis loops characteristic of ferrimagnetism at room temperature, with low coercivity (115 - 167 Oe) and negligible remanence, properties desirable for applications such as magnetic hyperthermia, MRI contrast agents, and drug delivery. The most significant result is the pronounced peak in Ms at pH 11. The sample synthesized under these conditions achieved Ms of 121.97 emu/g, the highest value observed in this study and competitive with values reported for maghemite nanoparticles prepared by similar routes [26,37]. This represents an enhancement of 20% - 25% compared with samples synthesized at pH 9 (101.06 emu/g), pH 10 (98.73 emu/g), and pH 12 (102.69 emu/g), demonstrating the effect of pH in optimizing magnetic properties. This enhancement can be attributed to favorable microstructural features at pH 11, which were observed as an average diameter of approximately 63 nm of nanoparticles, a size within the single domain regime for maghemite (20 - 80 nm). Particles in this size range are large enough to reduce surface spin disorder. The relatively spherical morphology at pH 11 exhibited an efficient magnetic coupling, whereas the irregular flakes at pH 12 hindered spin alignment. XRD confirmed that all samples crystallized as phase-pure maghemite with a constant primary crystallite size of about 24 nm. However, the effective crystallinity and defect density vary with pH, internal defects, and reduced lattice strain, enabling improved spin alignment. This is consistent with Filippousi *et al.* [37], who reported higher Ms in iron oxide nanoparticles synthesized under conditions that

minimize structural disorder. Surface spin disorder is also minimized at pH 11: The particle size is large enough to reduce surface-to-volume ratio effects but not so large that strain or surface passivation (e.g., by hydroxyl groups) becomes dominant, as at pH 12. The slight decrease in Ms at pH 12 is thus attributed to imperfections from anisotropic growth, such as internal strain and magnetically inactive surface layers. Coercivity (Hc) also varies with pH, reaching its maximum value of 166.75 Oe at pH 11. Higher Hc indicates stronger magnetic anisotropy, consistent with more uniform size and shape. The squareness ratio (R) also peaks at 0.26, suggesting enhanced inter-particle interactions. Although the samples exhibit non-zero coercivity and remanence, their low values (Hc < 170 Oe, Mr/Ms < 0.26) indicate behavior approaching superparamagnetism, which is suitable for biomedical applications where minimal residual magnetization is required [7]. Most notably, the anisotropy constant (K), calculated as reaching 21.18×10^3 emu·Oe/g at pH 11, is significantly higher than values at other pH conditions (12.11 - 13.46×10^3 emu·Oe/g). This provides strong evidence that pH 11 yields the most favorable balance of high Ms and strong anisotropy. Overall, pH 11 represents the optimal synthesis condition for maximizing magnetic performance in co-precipitated iron oxide nanomaterials. The enhancement does not arise from a phase change, but from pH-driven refinement of microstructure, ideal particle size, uniform morphology, and high crystalline order, all of which minimize spin disorder and maximize spin alignment. These findings align with broader literature showing that size, shape, and defect concentration govern magnetic properties in iron oxides [28,37,38]. The optimal pH may vary for other synthesis routes, such as the hydrothermal methods often favor pH 10 [39,40]. In contrast, this study found that pH 11 is the optimum condition for superior magnetic performance in the co-precipitation process.

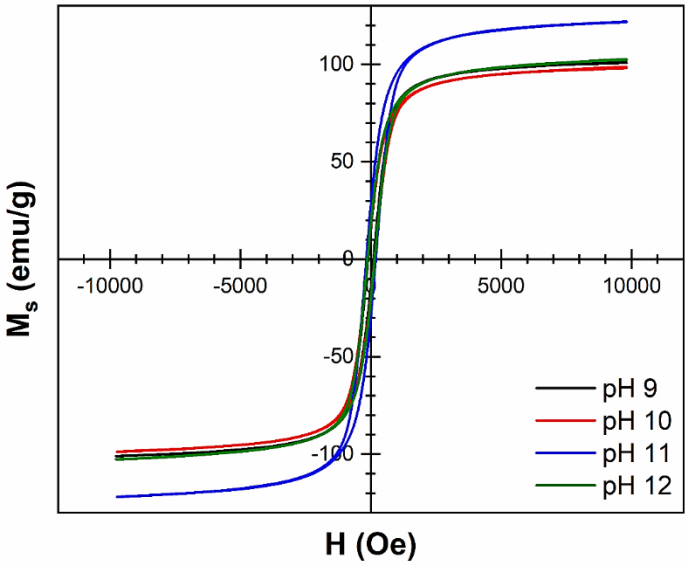

Figure 4 Magnetic hysteresis loops (VSM analysis) of iron oxide nanomaterials synthesized at pH 9 - 12.

Table 1 Magnetic parameters of iron oxide nanomaterials synthesized at pH 9 - 12 obtained from VSM analysis.

pH	Hc(Oe)	Ms (emu/g)	Mr (emu/g)	R = Mr/Ms	K(emu·Oe/g)
9	115.07	101.06	18.88	0.19	12.11×10^3
10	129.68	98.73	20.59	0.21	13.34×10^3
11	166.75	121.97	31.91	0.26	21.18×10^3
12	127.51	102.69	21.44	0.21	13.46×10^3

Thermal-induced phase transformation and grain growth

Calcination is a thermodynamic process that rearranges nanomaterials on atomic length scales and determines their morphology, crystal structure, phase stability, and functional properties. A distinct development from loosely packed amorphous-rich agglomerates through a stage of optimum crystallinity and particle definition up to a highly sintered and transformed phase structure is revealed by the gradual variation of the calcination temperature between 300 and 900°C. This evolution is revealed by complementary techniques, SEM for morphology and XRD for crystal structure, demonstrating the direct link between thermal history and material architecture, as shown in **Figures 5(a) - 5(d)**. At 300 °C, SEM shows a highly disordered network of small, irregular particles loosely aggregated with abundant voids. This indicates minimal atomic diffusion, consistent with incomplete structural maturation [41-44]. Such morphology provides high surface area, useful in catalysis, but is detrimental to applications requiring conductivity or mechanical stability. Raising the calcination temperature to 500 °C induces a dramatic transformation. Nanoparticles become more distinct, larger, and quasi-spherical. Loose aggregates consolidate into denser clusters, yet without excessive agglomeration. This balance reflects sufficient energy for enhanced crystalline and inter-particle connectivity, while still preserving surface accessibility. The morphology at 500 °C thus represents an optimal state, favorable for multifunctional applications such as catalysis, electronic transport, and magnetics [42-44]. At 700 °C, grain growth became the dominant process. Particles fuse into larger, irregular grains with rough surfaces and reduced porosity, hallmarks of early-stage sintering, where atom migration across grain boundaries minimizes surface energy [45]. At 900 °C, densification is further enhanced as nanoparticles grow into large, faceted grains with low porosity to form a solid microstructure. Although such a stage is mechanically sturdy, the surface area is reduced, and the generated internal stress can reduce its performance for applications in nanoscale [44].

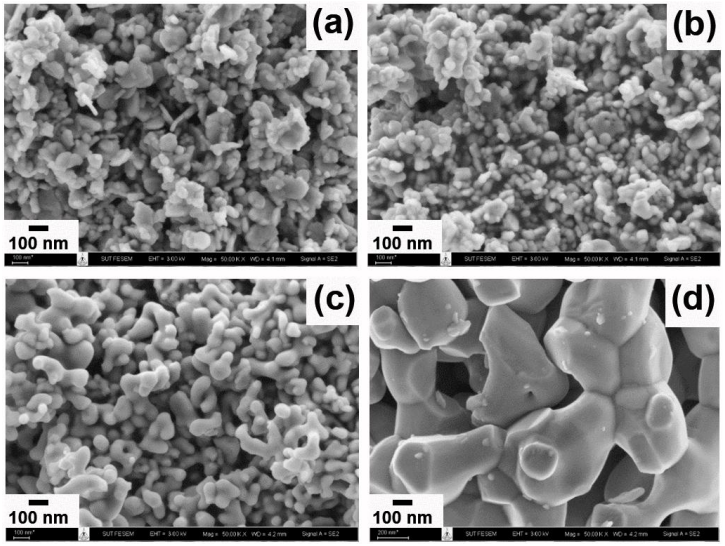

Figure 5 SEM images (50,000 magnification) of iron oxide nanomaterials calcined at temperatures of (a) 300, (b) 500, (c) 700 and (d) 900 °C.

This morphological evolution is also supported by XRD measurements (**Figure 6**) [41,42]. Diffraction peaks can be indexed to cubic maghemite (γ-Fe_2O_3, JCPDS No. 39-1346) only at 300 and 500 °C. The 300 °C peaks are broad compared to the 500 °C samples, but still weak, indicating small crystallite sizes and lattice defects, whereas at 500 °C, peaks sharpen concomitantly with higher crystallinity and larger crystallites [43,44] but on the other hand, followed by a sharpening of the reflections at 500 °C, suggesting an increased crystallinity with larger grains. A significant transition takes place from 500 to 700 °C with the

emergence of new reflections corresponding to rhombohedral hematite (α-Fe_2O_3, JCPDS No. 33-664) [45]. The onset of hematite formation at 700 °C aligns with Bora *et al.* [45], who reported a similar transition in air-annealed γ-Fe_2O_3 nanoparticles. Here, these maxima increase with increasing temperature (T), indicating almost full transformation to hematite upon reaching 900 °C as the phase change is thermodynamically necessary. Maghemite is a metastable form, and the stable Fe^{3+} oxide under high temperature and ambient oxygen is the mineral hematite. Calcination provides enough heat for overcoming the kinetic barrier of arranging structure, transferring the defect-spinel constructed framework of maghemite to the corundum structure of hematite [45]. This reveals that the calcination temperature controls the nature and characteristics of iron oxide nanomaterials [41-45]. At 300 °C, the structure is underdeveloped and disordered. The best condition showing high crystallinity, clear morphology, and presence of the preferable γ-Fe_2O_3 phase is at 500 °C. Beyond this size range, overgrowth of the grains, densification, and phase transformation to hematite impairs performance. Thereby, this 500 °C appears to be the golden temperature where thermal energy enriches the structure without losing phase stability. In contrast to pH, which only affects morphology, calcination temperature governs phase stability and induces irreversible structural transformation.

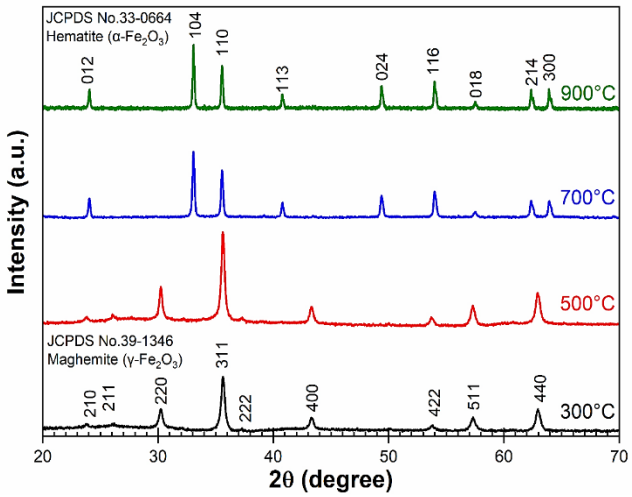

Figure 6 XRD patterns of iron oxide nanomaterials calcined at temperatures of 300 - 900 °C.

Raman spectroscopic analysis of thermally driven phase evolution

The Raman spectra (**Figure 7**) provide for the crystal structure evolution of the co-precipitated iron oxide nanoparticles under varying calcination temperatures from 300 to 900 °C, which supported XRD data and provided further understanding of phase transformation mechanisms. At 300 °C (black line), the spectrum is characterized by peaks at ~211, 271, 383, 474, and 578 cm^{-1} typical for maghemite (γ-Fe_2O_3) with a spinel structure featuring cation vacancies [45]. Lattice disorder, fine crystallite size, and residual defects such as hydroxyl groups are presented by broad low-intensity peaks [45]. At 500 °C (red line), these peaks increase in sharpness and height, especially the doublet around ~211 and ~271 cm^{-1}. This enhancement indicates an increase in crystallinity, a decrease in lattice strain, and the recovery of point defects, whereas the peak position is not changed, indicating that the material is still crystalline γ-Fe_2O_3. There is a substantial change at 700 °C (blue line). The maghemite peaks vanish and new peaks arise at 215, 281, 395, 487, and 588 cm^{-1}, which is the representative fingerprint of hematite (α-Fe_2O_3) with corundum structure [45-47]. The abrupt changeover is indicative of a reconstructive phase transition, which can plausibly be assumed to be controlled by the thermodynamic stability of hematite at high temperature [44,45]. When the temperature reaches 900 °C (green curve), hematite peaks are observed to be more intense and sharper, indicating high crystalline quality, a low number of defects, and a larger crystallite size. Raman spectroscopy hereby establishes a clear

temperature-induced progression: disordered γ-Fe_2O_3 at 300 °C, highly crystalline γ-Fe_2O_3 at 500 °C, and full α-Fe_2O_3 exotherm above 700 °C. This structural understanding is essential for interpreting the optical, magnetic, and electrical data discussed in further analyses.

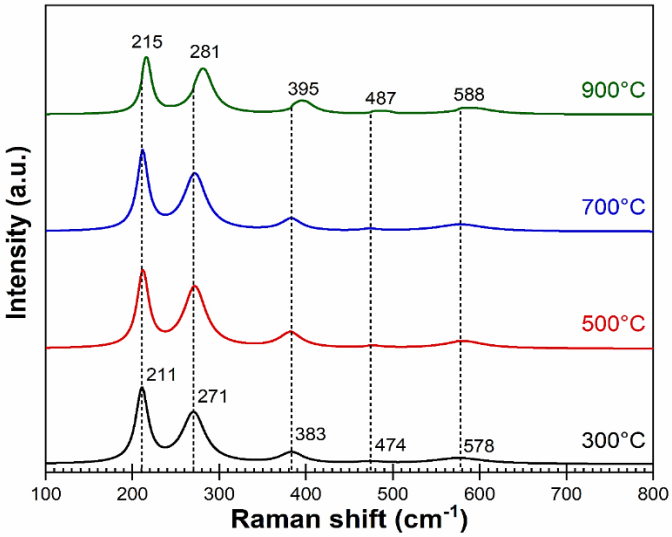

Figure 7 Raman spectra of iron oxide nanomaterials calcined at temperatures of 300 - 900 °C.

Thermal evolution of defect states and optical band gap by fluorescence spectroscopy

The fluorescence spectra (**Figure 8(a)**) were deconvoluted using Lorentzian fitting to resolve overlapping emission bands [48,49]. Three primary regions of emission are consistently observed across all calcination temperatures, each corresponding to a distinct type of electronic transition. A violet emission band, centered in the wavelength range of approximately 305 to 325 nm (corresponding to photon energies of 3.82 to 4.05 eV), is attributed to near-band-edge (NBE) recombination. This high-energy emission arises from the direct radiative recombination of electrons in the conduction band with holes in the valence band, providing a measure of the material's fundamental band gap [49,50]. At longer wavelengths, a blue emission band is observed, centered between 415 and 454 nm (2.73 to 2.98 eV). This emission is strongly associated with radiative transitions involving shallow defect states, most notably oxygen vacancies (V_O) [51,52]. These defects act as electron traps, creating discrete energy levels within the band gap that facilitate non-radiative recombination via a lower-energy pathway. The significant quenching of this emission at higher calcination temperatures (700 and 900 °C) provides direct evidence for the thermal annihilation of these oxygen vacancy sites, which is consistent with the observed increase in crystallinity and phase purity confirmed by XRD and Raman analyses [49,53,54].

This behavior aligns with studies demonstrating that oxygen vacancies are highly mobile at elevated temperatures and can be effectively passivated through atomic diffusion and lattice reconstruction [55,56]. Furthermore, the presence of interstitial iron atoms (Fe_i) may also contribute to the blue emission, particularly through Fe^{2+}/Fe^{3+} charge transfer transitions, which are known to produce visible luminescence in iron oxides [51,57]. The reduction in overall fluorescence intensity with increasing temperature suggests a decrease in the concentration of both types of defects, reinforcing the conclusion that thermal annealing promotes structural ordering and defect healing [58,59]. Finally, a long-wavelength emission band appears in the green region of the spectrum, centered at 559 to 579 nm (2.14 to 2.22 eV). This lower-energy emission is linked to deep-level defects and complex recombination processes, often involving surface states or intricate defect clusters. The presence of this band is frequently indicative of a higher degree of structural disorder or a larger surface-to-volume ratio, where broken bonds and unsaturated sites create a manifold of energy levels deep within the band gap [60].

The most significant and consistent trend observed across all 3 emission bands is the systematic and

substantial reduction in fluorescence intensity with increasing calcination temperature. The spectra at 300 °C are characterized by intense and broad emission features, signaling a high density of radiative recombination centers, primarily defects. As the temperature increases to 500 °C, the intensity begins to diminish. By 700 and 900 °C, the fluorescence is dramatically quenched, becoming almost negligible at the highest temperature [61,62]. This quenching is a direct manifestation of the thermal annealing process. The elevated temperatures provide the activation energy required for atomic diffusion, enabling the material to annihilate point defects, heal lattice imperfections, and drive the phase transformation to the more structurally rigid hematite phase [49,56]. The near-complete disappearance of luminescence at 900 °C is thus a clear indicator of the material's attainment of a high degree of crystalline perfection and phase purity [63]. Crucially, the optical band gap (Eg) for each emission band, calculated using the relation:

$$Eg = 1240/\lambda \text{ (eV)} \quad (6)$$

where λ is the peak wavelength in nanometers [24], exhibits a clear and significant increase with calcination temperature, as quantitatively displayed in **Figure 8(b)**.

It should be noted that the band gap values derived from fluorescence emission peaks represent effective optical gaps influenced by defect states and are distinct from the fundamental band gap obtained via Tauc plot analysis of UV-Vis data. For example, the energy associated with the blue emission peak shifts from approximately 2.73 eV at 300 °C to 2.98 eV at 900 °C. This upward shift in emission energy is entirely consistent with the defect annihilation model. Defects, particularly oxygen vacancies, introduce mid-gap states that effectively create lower-energy pathways for electronic transitions, thereby narrowing the observed optical band gap. As these defects are progressively removed during thermal annealing, the mid-gap states are eliminated. Consequently, electronic transitions are forced to occur across the material's intrinsic band gap, which is wider. The phase transition from maghemite (intrinsic band gap ~2.0 eV) to hematite (intrinsic band gap ~2.2 eV) further contributes to this overall widening of the effective band gap for radiative transitions [13,64].

Thermal treatment orchestrates a fundamental transformation in the optical character of iron oxide nanomaterials. At low temperatures, the material is optically active, emitting brightly due to a high concentration of defects that serve as efficient luminescent centers. As temperature increases, thermal energy acts to heal these imperfections and drive a phase transition, resulting in a material that is structurally pristine but optically inert. The optimal point for applications that require a balance between defect-mediated functionality and structural stability is found at 500 °C. At this temperature, the material retains sufficient defect density for useful luminescence while exhibiting improved crystallinity. Beyond this point, the pursuit of thermodynamic equilibrium leads to a material that has sacrificed its optically active defects for crystalline perfection, a trade-off that must be carefully considered for any intended application.

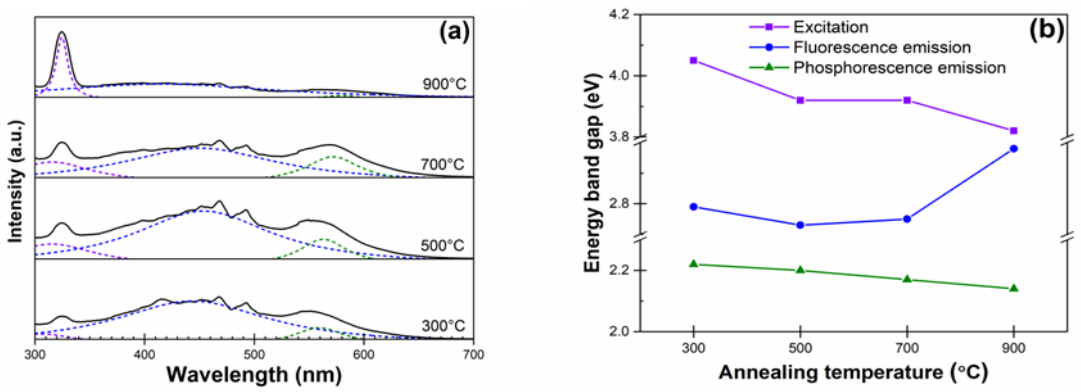

Figure 8 (a) Main fluorescence spectrum (black line) deconvoluted into 3 components using Lorentzian fitting (blue, green, and red lines); (b) Energy band gap values derived from the 3 Lorentzian peaks of iron oxide nanomaterials calcined at temperatures ranging from 300 - 900 °C.

Calcination temperature-dependent magnetic performance

The magnetic journey begins at the lowest calcination temperature of 300 °C. The hysteresis loop (**Figure 9**) for this sample exhibits a characteristic S-shape with a saturation magnetization (Ms) of 58.18 emu/g and a coercivity (Hc) of 191.61 Oe. The squareness ratio (R) is 0.28, indicating a multi-domain magnetic structure, which has undergone initial oxide formation but retains a high degree of structural imperfection. The relatively low Ms is attributed to a combination of factors: Small crystallite size (as indicated by broad XRD peaks in **Figure 6**), a high surface-to-volume ratio leading to significant surface spin disorder, and the possible presence of residual non-magnetic phases or hydroxyl groups. The spins at the surface of these small particles are often disordered due to broken symmetry and unsaturated bonds, which prevent them from contributing coherently to the net magnetization [63].

As the calcination temperature has increased to 500 °C, a remarkable and highly beneficial transformation occurs. The Ms undergoes a dramatic increase, reaching its peak value of 115.61 emu/g. This represents nearly a doubling of the magnetization compared to the 300 °C sample and is one of the highest values reported for maghemite nanoparticles synthesized via co-precipitation. Concurrently, the Hc slightly decreases to 150.41 Oe, and the R value reduces to 0.24. This combination of high Ms, moderate Hc, and low R is the hallmark of an optimized magnetic material which signifies the development of a uniform single-domain-like particle structure and more efficient under an applied field The significant enhancement in Ms is directly attributable to the improvements in microstructure observed at this temperature: increased crystallinity (sharper XRD and Raman peaks), larger and more well-defined particle size (SEM, **Figure 5**), and a consequent reduction in the detrimental effects of surface spin disorder [56,57,59,63]. The calcination at 500 °C is sufficient to heal point defects, reduce lattice strain, and atomic ordering, which contribute to a robust and coherent magnetic response. While the non-zero Hc and R values preclude a strict classification as superparamagnetic (which requires Hc ≈ 0 Oe and R ≈ 0), the behavior at 500 °C can be aptly described as near-superparamagnetic or pseudo-superparamagnetic. This state is ideal for applications such as magnetic hyperthermia and targeted drug delivery, where a strong magnetic response is needed to manipulate the particles, but minimal residual magnetism is required to prevent aggregation once the field is removed [58,60,61]. The magnetic moment (μB), a fundamental measure of the magnetic strength per formula unit, was calculated from the Ms value. At 500 °C, it reaches its maximum, further confirming the peak in magnetic ordering. The anisotropy constant (K) value also peaks at this temperature, indicating the strong magnetic anisotropy, used for the stability of the magnetic domains against thermal fluctuations. This state of magnetic excellence is, however, ephemeral. Beyond 500 °C, the relentless increase in thermal energy triggers a fundamental and irreversible change in the material's identity.

At 700 and 900 °C, the magnetic performance undergoes a catastrophic collapse. The Ms decreases to 0.76 emu/g and 0.77 emu/g, respectively, a reduction of over 99 % compared to the 500 °C sample. This is not a gradual decline but a near-total annihilation of the ferrimagnetic order. Simultaneously, the Hc increases dramatically to 1,084.61 and 1,242.02 Oe, and the R value rises to 0.42 and 0.45. This inverse relationship, where Ms collapses while Hc soars, is the unmistakable fingerprint of a phase transition from ferrimagnetic maghemite (γ-Fe_2O_3) to antiferromagnetic hematite (α-Fe_2O_3), as definitively confirmed by XRD (**Figure 6**) and Raman analyses (**Figure 7**) [62]. Hematite (α-Fe_2O_3) possesses a corundum structure where the Fe^{3+} ions are arranged in such a way that their magnetic moments couple antiparallel to each other, resulting in a net zero magnetization in its ideal, bulk form. However, at the nanoscale and in imperfect crystals, hematite can exhibit very weak ferromagnetism or parasitic ferromagnetism due to spin canting or defects [61,64]. The observed low Ms and very high Hc at 700 and 900 °C are consistent with this weakly ferromagnetic state of hematite. The high coercivity arises from the large magnetocrystalline anisotropy of the hematite phase and the formation of large, multi-domain grains, as seen in the SEM images (**Figure 5**). The increase in R value suggests a squarer hysteresis loop, which is typical for materials with high anisotropy and domain wall pinning. The anisotropy constant (K) follows this trend of

collapse, decreasing precipitously from its peak at 500 °C to negligible values at 900 °C. This reflects the loss of the long-range ferrimagnetic order that characterized the maghemite phase. The spins in hematite are locked in an antiparallel configuration, and the energy barrier for magnetization reversal (which K represents) becomes irrelevant in the context of a material with no net spontaneous magnetization.

The calcination temperature exerts an extraordinary level of control over the magnetic destiny of iron oxide nanomaterials. It was noted that the reached a zenith of magnetic performance, achieving a near-superparamagnetic state with maximum saturation magnetization at 500 °C, making it ideal for advanced biomedical and technological applications. Any further increase in temperature, however, initiates a thermodynamically driven phase transition to hematite, which acts as a magnetic off switch, reducing the material to a state of near-zero magnetization [53,54,57]. This profound understanding allows for the precise thermal programming of magnetic properties, with 500 °C standing as the unequivocal optimum temperature for maximizing magnetic functionality.

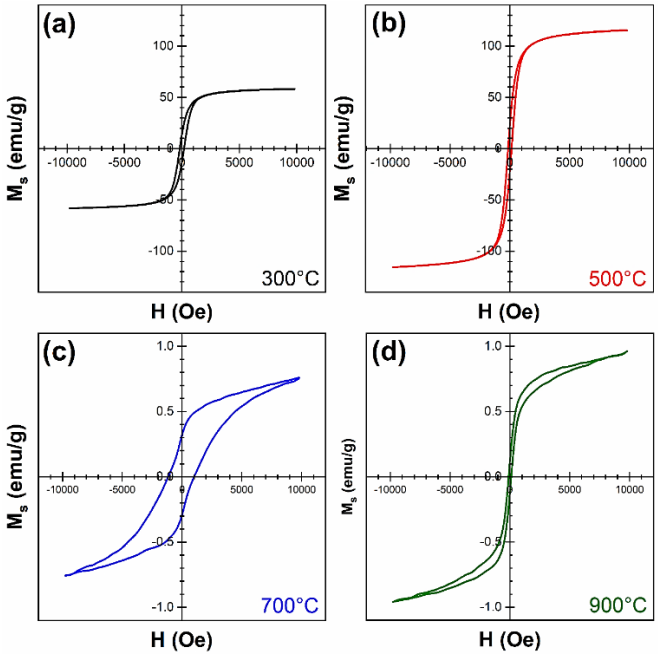

Figure 9 Magnetic hysteresis loops of iron oxide nanomaterials calcined at temperatures of 300 - 900 °C.

Temperature-dependent electrical conductivity

The results (**Figure 10**) plotted a dependence of resistance (R), resistivity (ρ), and conductivity (σ) on calcination temperature. At the lowest calcination temperature of 300 °C, the material exhibits a relatively high electrical resistance of 0.4956 MΩ. This elevated resistance translates to a high resistivity of 49.56×10^{6} Ω·cm, indicating that charge carriers encounter significant obstacles to their movement. This behavior is entirely consistent with the material's immature state at this temperature. XRD patterns (**Figure 6**) reveal broad, low-intensity diffraction peaks, signifying small crystallite size (~24 nm) and a high density of lattice defects and strain. SEM images (**Figure 5**) show a loosely aggregated, porous morphology, which forces charge carriers to traverse numerous high-resistance inter-particle junctions. The intense defect-related fluorescence observed at this temperature (**Figure 8**) further corroborates this picture, as deep-level traps can capture and immobilize charge carriers, effectively removing them from the conduction process.

As the calcination temperature is elevated to 500 °C, a dramatic transformation in electrical performance occurs. The resistance undergoes a sharp, 5-fold decrease, plummeting to a minimum value of 0.1014 MΩ. This corresponds to a peak in electrical conductivity, unequivocally establishing 500 °C as the optimal temperature for charge transport. The calculated conductivity reaches its maximum value of 98.62×10^{-9} $(\Omega\cdot cm)^{-1}$, marking a nearly 5-fold enhancement

compared to 300 °C. This improvement is attributable to an enhancement in structural order, which corresponds XRD peaks becoming sharp and intense (**Figure 6**), confirming an increase in crystallinity and a reduction in lattice defects and strain. SEM images (**Figure 5**) reveal more distinct nanoparticles forming denser, interconnected aggregates, creating efficient percolation pathways for current. Fluorescence spectra (**Figure 8**) also show quenching of defect-related emissions, indicating a reduction in carrier-trapping states. Collectively, these findings confirm that the superior conductivity at 500 °C arises from improved crystallinity and particle connectivity rather than mixed-valence conduction, since the phase remains maghemite (γ-Fe_2O_3) [58].

Beyond this optimum, electrical performance undergoes steady degradation. At 700 °C, the resistance was increased to 0.1466 MΩ, and at 900 °C it rose to 0.1592 MΩ (meaning considerably high resistivity from 10.14×10^6 to 15.92×10^6 Ω·cm) and low conductivity (from 98.62×10^{-9} to 62.81×10^{-9} $(\Omega\cdot cm)^{-1}$). This degradation correlates directly with the phase transition from maghemite to hematite, as clearly indicated by XRD (**Figure 6**) and Raman spectra (**Figure 7**) [59]. Hematite is an n-type semiconductor with a band gap of ~2.2 eV and inherently lower conductivity due to the absence of Fe^{2+} ions, which in magnetite enable electron hopping [60,61]. The massive grain growth and densification observed at 900 °C (**Figure 5**), while reducing macroscopic porosity, do not compensate for this fundamental loss of electronic mobility. In fact, the formation of large grains introduces new, resistive grain boundaries that further impede conduction [59,60]. The electrical conductivity (σ) is the inverse of resistivity (ρ), defined as:

$$\sigma = 1/\rho \quad (7)$$

which

$$\rho = RA/L \quad (8)$$

This relationship is evident in **Figure 10**, where the conductivity curve (blue) mirrors the resistivity curve (red). The calcination temperature exerts exquisite control over the electrical functionality of iron oxide nanomaterials. At 300 °C, structural disorder renders the material a poor conductor. At 500 °C, thermal energy is optimally harnessed to perfect the maghemite structure, heal defects, and improve particle connectivity, yielding peak conductivity. Any further increase in temperature triggers the transformation to hematite, which acts as an electrical off switch, drastically reducing charge transport. Notably, this optimum at 500 °C coincides with the peak magnetic (**Figure 9**) and balanced optical (**Figure 8**) performance, firmly establishing it as the optimum condition for multifunctional performance in co-precipitated iron oxide nanomaterials [64]. A comprehensive summary of the thermal evolution of structural and functional properties is provided in **Table 2**.

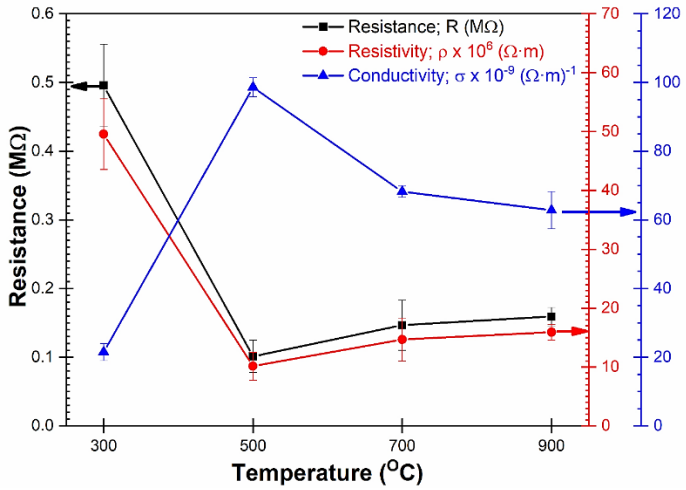

Figure 10 Electrical resistance, resistivity, and conductivity of iron oxide nanomaterials calcined at temperatures of 300 - 900 °C.

Table 2 Summary of structural, optical, electrical, and magnetic properties of iron oxide nanomaterials synthesized at pH 11 and calcined at different temperatures.

Calcination Temp. (°C)	Crystal Phase	Crystallite Size (nm)	Ms (emu/g)	Eg (eV)	σ ($\times10^{-9}$ $(\Omega\cdot cm)^{-1}$)
300	γ-Fe_2O_3	24	58.18	2.73	20.2
500	γ-Fe_2O_3	28	115.61	2.03	98.62
700	α-Fe_2O_3	55	0.76	2.98	68.2
900	α-Fe_2O_3	110	0.77	2.98	62.81

*Eg from fluorescence (Section 6)-use the blue emission peak value.

Conclusions

This work investigates the synthesis pH (9 - 12) and calcination temperature (300 - 900 °C) that govern the structural, optical, electrical, and magnetic properties of co-precipitated iron oxide nanomaterials. The pH influenced particle size, morphology, and magnetic response without altering the crystal phase, whereas calcination temperature affected crystallinity, defect chemistry, and phase stability. All samples synthesized across pH 9 - 12 crystallized as γ-Fe_2O_3. The condition at pH 11 produced the most uniform nanoparticles and the highest magnetization, attributed to reduced surface spin disorder, a value surpassing recent co-precipitated systems (e.g., 101 - 102 emu/g [26,37]). The narrow indirect band gap of 2.03 eV aligns with the intrinsic gap of maghemite and is advantageous over wider-gap hematite systems (~2.2 eV) for visible-light photocatalysis [13]. The optimum crystallinity, reduced defect density, and enhanced particle agglomeration resulted in peak electrical conductivity and near-superparamagnetic magnetic behavior, are shown at 500 °C, which presents the optimal structural and defect-related functionality, promising for multifunctional applications. However, further heating drives a reconstructive phase transition from maghemite to hematite between 500 and 700 °C. The transformation leads to a collapse in magnetic performance and increased resistivity, consistent with the antiferromagnetic and semiconducting character of hematite. Critically, the combined optimization of pH and calcination identifies pH 11 at 500 °C as the optimal condition, where morphology, crystallinity, magnetization, and conductivity are simultaneously maximized. Such a 2-parameter control behavior offers an experimentally demonstrated methodology to design balanced multifunctional iron oxide nanomaterials. Therefore, this knowledge supports their inclusion in high-technology devices such as spintronic devices, multi-functional biomedical platforms, and catalytic systems.

Acknowledgements

The authors acknowledge the support provided by Nakhon Ratchasima Rajabhat University, Nakhon Ratchasima, Thailand, for the experimental facilities and funding assistance. I would like to thank Khajondach Viangsong and Napaporn Thaweesaeng for their assistance with the preparation and analysis of UV-VIS spectroscopy and electrical resistance measurements. The XRD measurements and fluorescence spectroscopy were supported by Dr. Panadda Phansamdaeng, with contributions from Samart Tuaykratok.

Declaration of generative AI in scientific writing

This manuscript utilized generative AI tools, namely Qwen, ChatGPT (OpenAI), and Grammarly were used during the preparation of this manuscript solely for language editing, grammar correction, and structural suggestions. All scientific content, data interpretation, experimental design, and final wording decisions were made exclusively by the author. The use of AI complies with the ethical guidelines for scientific publishing. The authors affirm that they are fully responsible for the intellectual content, scientific accuracy, and integrity of this manuscript.

CRediT author statement

Buppachat Toboonsung: Conceptualization, Methodology, Software, Validation, Formal analysis,

Investigation, Resources, Data curation, Writing - original draft, Writing - review & editing, Visualization, Supervision, Project administration, Funding acquisition.

References

[1] H Gleiter. Nanostructured materials: Basic concepts and microstructure. *Acta Materialia* 2000; **4(1)**, 1-29.

[2] JE Ogbezode, US Ezealigo, A Bello, VC Anye and AP Onwualu. A narrative review of the synthesis, characterization, and applications of iron oxide nanoparticles. *Discover Nano* 2023; **18**, 125.

[3] AK Gupta and M Gupta. Synthesis and surface engineering of iron oxide nanoparticles for biomedical applications. *Biomaterials* 2005; **26(18)**, 3995-4021.

[4] DS Chaudhari, RP Upadhyay, GY Shinde, MB Gawande, J Filip, RS Varma and R Zbořil. A review on sustainable iron oxide nanoparticles: Synthesis and application in organic catalysis and environmental remediation. *Green Chemistry* 2024; **26**, 7579-7655.

[5] S Laurent, D Forge, M Port, A Roch, C Robic, LV Elst and RN Muller. Magnetic iron oxide nanoparticles: Synthesis, stabilization, vectorization, physicochemical characterizations, and biological applications. *Chemical Reviews* 2008; **108(6)**, 2064-2110.

[6] AH Lu, EL Salabas and F Schüth. Magnetic nanoparticles: Synthesis, protection, functionalization, and application. *Angewandte Chemie International Edition* 2007; **46(8)**, 1222-1244.

[7] MA Gabal, A Alshammari, H Alotaibi and S Alharbi. Cytotoxicity and hemostatic 1 step green synthesis of iron nanoparticles coated with green tea for biomedical application. *Trends in Sciences* 2022; **19(3)**, 2062.

[8] J Yuennan, N Muensit, N Tohluebaji, W Chailad, L Yang, N Sukhawipat, GA Ashraf and P Channuie. Tailoring dielectric properties and crystallinity in poly(vinylidene fluoride-co-hexafluoropropylene) nanocomposites via iron (III) chloride hexahydrate incorporation. *Scientific Reports* 2025; **15**, 17810.

[9] J Yuennan, S Al-Sulaimi, M Karimov, A Abduvokhidov, M Mirzayev, GA Ashraf, Z Javed, A Ayari-Akkari, RM Ali, A Guesmi and P Channuie. Photocatalytic degradation of tetracycline via peroxymonosulfate activation via $W_{0.5}Ag_{0.5}FeO_3$: A synergistic approach for sustainable water treatment. *Vacuum* 2025; **241**, 114639.

[10] N Lertcumfu, FN Sayed, SN Shirodkar, S Radhakrishnan, A Mishra, G Rujijanagul, AK Singh, BI Yakobson, CS Tiwary and PM Ajayan. Structure-dependent electrical and magnetic properties of iron oxide composites. *Physica Status Solidi (A)* 2019; **216(16)**, 1801004.

[11] S Singh and N Goswami. Structural, magnetic and dielectric study of Fe_2O_3 nanoparticles obtained through exploding wire technique. *Current Applied Physics* 2021; **20**, 20-29.

[12] YP Yew, K Shameli, M Miyake, NBBA Khairudin, SEB Mohamad, T Naiki and KX Lee. Green biosynthesis of superparamagnetic magnetite Fe_3O_4 nanoparticles and biomedical applications in targeted anticancer drug delivery system: A review. *Arabian Journal of Chemistry* 2020; **13(1)**, 2287-2308.

[13] K Sivula, FL Formal and M Grätzel. Solar water splitting: Progress using hematite (α-Fe_2O_3) photoelectrodes. *ChemSusChem* 2011; **4(4)**, 432-449.

[14] W Wu, Q He and X Zhong. Magnetic iron oxide nanoparticles: Synthesis and surface functionalization strategies. *Nanoscale Research Letters* 2008; **3**, 397-415.

[15] S Sun, H Zeng, DB Robinson, S Raoux, PM Rice, SX Wang and G Li. Monodisperse MFe_2O_4 (M = Fe, Co, Mn) nanoparticles. *Journal of the American Chemical Society* 2004; **126(1)**, 273-279.

[16] M Unni, AM Uhl, S Savliwala, BH Savitzky, R Dhavalikar, N Garraud, DP Arnold, LF Kourkoutis, JS Andrew and C Rinaldi. Thermal decomposition synthesis of iron oxide nanoparticles with diminished magnetic dead layer by controlled addition of oxygen. *ACS Nano* 2017; **11(2)**, 2284-2303.

[17] MO Besenhard, AP LaGrow, A Hodzic, M Kriechbaum, L Panariello, G Bais, K Loizou, S

Damilos, MM Cruz, NTK Thanh and A Gavriilidis, Co-precipitation synthesis of stable iron oxide nanoparticles with NaOH: New insights and continuous production via flow chemistry. *Chemical Engineering Journal* 2020; **399**, 125740.

[18] Y Lu, Y Yin, BT Mayers and Y Xia. Modifying the surface properties of superparamagnetic iron oxide nanoparticles through a sol-gel approach. *Nano Letters* 2002; **2(3)**, 183-186.

[19] A Ghosh, V Srinivas and R Sundara. Comprehensive structural and magnetic properties of iron oxide nanoparticles synthesized through chemical routes. *Journal of Alloys and Compounds* 2020; **818**, 152931.

[20] VG Ilves, N Pizúrová, PM Korusenko, SY Sokovnin, ME Balezin, AS Gerasimov, MA Uimin, MG Zuev and AA Vasin. Effect of air annealing on properties of maghemite nanoparticles produced by radiation-chemical method. *Ceramics International* 2023; **49(15)**, 25414-25426.

[21] A Lassoued, MS Lassoued, B Dkhil, S Ammar and A Gadri. Synthesis, photoluminescence and magnetic properties of iron oxide (α-Fe_2O_3) nanoparticles through precipitation or hydrothermal methods. *Physica E: Low-dimensional Systems and Nanostructures* 2018; **101**, 212-219.

[22] Ritik, S Sarkar, Pragti, N Varshney, A Kumar, ML Kuznetsov, HC Jha and S Mukhopadhyay. Nano-Structured Gel Materials for Environmental Remediation and Biomedical Applications. *ACS Applied Nano Materials* 2024; **7(18)**, 22292-22303.

[23] W Wu, Z Wu, T Yu, C Jiang and WS Kim. Recent progress on magnetic iron oxide nanoparticles: synthesis, surface functional strategies and biomedical applications. *Science and Technology of Advanced Materials* 2015; **16**, 023501.

[24] P Kingpho and B Toboonsung. Improvement of the electrical properties of ZnO nanomaterials with Fe by co-precipitation method. *Current Applied Science and Technology* 2025; **25(3)**, e0263485.

[25] B Toboonsung. Structure, magnetic property and energy band gap of Fe-doped NiO nanoparticles prepared by co-precipitation method. *Key Engineering Materials* 2017; **751**, 379-383.

[26] F Naushin, S Sen, M Kumar, H Bairagi, S Maiti, J Bhattacharya and S Sen. Structural and surface properties of pH-varied Fe_2O_3 nanoparticles: Correlation with antibacterial properties. *ACS Omega* 2024; **9(1)**, 464-473.

[27] FN Sayed and V Polshettiwar. Facile and sustainable synthesis of shaped iron oxide nanoparticles: Effect of iron precursor salts on the shapes of iron oxides. *Scientific Reports* 2015; **5**, 9733.

[28] A Adel, R Locif, BI Yaacoub, H Abdelmadjid, R Selma and B Imed-Eddine. pH-dependent deposition of Cu_2O thin films: Tuning defect states and electronic properties for improved energy conversion applications. *Applied Physics A* 2025; **131(105)**, 1-21.

[29] B Choudhury, S Bayan, A Choudhury and P Chakraborty. Narrowing of band gap and effective charge carrier separation in oxygen-deficient TiO_2 nanotubes with improved visible light photocatalytic activity. *Journal of Colloid and Interface Science* 2016; **465**, 1-10.

[30] N Tohluebaji, R Siri, N Muensit, C Putson, P Channuie,P Porrawatkul and J Yuennan. Hydrophobic and optical properties of p(vdf-hfp)nanofiber filled with nickel (ii) chloride hexahydrate for dye-sensitized solar cells application. *Trends in Sciences* 2024; **21(9)**, 8762.

[31] VB Kamble and AM Umarji. Defect induced optical bandgap narrowing in undoped SnO_2 nanocrystals. *AIP Advances* 2013; **3(8)**, 082120.

[32] JC Mora, YCM Nederstigt, JM Hill and S Ponnurangam. Promoting effect of supports with oxygen vacancies as extrinsic defects on the reduction of iron oxide. *The Journal of Physical Chemistry C* 2021; **125(26)**, 14299-14310.

[33] J Wang, Z Wang, B Huang, Y Ma, Y Liu, X Qin, X Zhang and Y. Dai. Oxygen vacancy induced band-gap narrowing and enhanced visible light photocatalytic activity of ZnO. *ACS Applied Materials & Interfaces* 2012; **4(8)**, 4024-4030.

[34] P Kushwaha and P Chauhan. Influence of different surfactants on morphological, structural, optical, and magnetic properties of α-Fe_2O_3 nanoparticles

synthesized via co-precipitation method. *Applied Physics A* 2022; **128(18)**, 1-14.

[35] D Nadhiya, A Kala, P Sasikumar, MKA Mohammed, P Thirunavukkarasu, M Prabhaharan, C Karnan, S Albukhaty, MS Jabir, A Syed, AM Elgorban and NSS Zaghloul. Influence of Cu^{2+} substitution on the structural, optical, magnetic, and antibacterial behaviour of zinc ferrite nanoparticles. *Journal of Saudi Chemical Society* 2023; **27(5)**, 101696.

[36] MM Arman and SI El-Dek. Structural, surface, magnetic study and application of nanoparticles $CoFe_2O_4$, ZnO and its nanocomposite. *Journal of Superconductivity and Novel Magnetism* 2023; **36**, 1913-1925.

[37] M Filippousi, M Angelakeris, M Katsikini, E Paloura, I Efthimiopoulos, Y Wang, D Zamboulis and G Van Tendeloo. Surfactant effects on the structural and magnetic properties of iron oxide nanoparticles. *The Journal of Physical Chemistry C* 2014; **118(29)**, 16209-16217.

[38] X Batlle, C Moya, M Escoda-Torroella, Ò Iglesias, AF Rodríguez and A Labarta. Magnetic nanoparticles: From the nanostructure to the physical properties. *Journal of Magnetism and Magnetic Materials* 2022; **543**, 168594.

[39] A Lassoued, MS Lassoued, B Dkhil, S Ammar and A Gadri. Synthesis, structural, morphological, optical and magnetic characterization of iron oxide (α-Fe_2O_3) nanoparticles by precipitation method: Effect of varying the nature of precursor. *Physica E: Low-dimensional Systems and Nanostructures* 2018; **97**, 328-334.

[40] ACB Jesus, JR Jesus, RJS Lima, KO Moura, JMA Almeida, JGS Duque and CT Meneses. Synthesis and magnetic interaction on concentrated Fe_3O_4 nanoparticles obtained by the co-precipitation and hydrothermal chemical methods. *Ceramics International* 2020; **46(8)**, 11149-11153.

[41] APA Faiyas, EM Vinod, J Joseph, R Ganesan and RK Pandey. Dependence of pH and surfactant effect in the synthesis of magnetite (Fe_3O_4) nanoparticles and its properties. *Journal of Magnetism and Magnetic Materials* 2010; **322(4)**, 400-404.

[42] J Lei, Z Luo, S Qing, X Huang and F Li. Effect of surfactants on the stability, rheological properties, and thermal conductivity of Fe_3O_4 nanofluids. *Powder Technology* 2022; **399**, 117197.

[43] AR Chakraborty, FTZ Toma, K Alam, SB Yousuf and KS Hossain. Influence of annealing temperature on Fe_2O_3 nanoparticles: Synthesis optimization and structural, optical, morphological, and magnetic properties characterization for advanced technological applications. *Heliyon* 2024; **10(21)**, e40000.

[44] P Kushwaha and P Chauhan. Influence of annealing temperature on microstructural and magnetic properties of Fe_2O_3 nanoparticles synthesized via sol-gel method. *Inorganic and Nano-Metal Chemistry* 2022; **52(7)**, 937-950.

[45] DK Bora, A Braun, S Erat, O Safonova, T Graule and EC Constable. Evolution of structural properties of iron oxide nanoparticles during temperature treatment from 250 °C - 900 °C: X-ray diffraction and Fe K-shell pre-edge X-ray absorption study. *Current Applied Physics* 2012; **12(3)**, 817-825.

[46] E Darezereshki, F Bakhtiari, M Alizadeh, AB Vakylabad and M Ranjbar. Direct thermal decomposition synthesis and characterization of hematite (α-Fe_2O_3) nanoparticles. *Materials Science in Semiconductor Processing* 2012; **15(1)**, 91-97.

[47] A Lassoued, MS Lassoued, B Dkhil, A Gadri and S Ammar. Synthesis, structural, optical and morphological characterization of hematite through the precipitation method: Effect of varying the nature of the base. *Journal of Molecular Structure* 2017; **1141(5)**, 99-106.

[48] M Cho, EQ Contreras, SS Lee, CJ Jones, W Jang and VL Colvin. Characterization and optimization of the fluorescence of nanoscale iron oxide/quantum dot complexes. *The Journal of Physical Chemistry C* 2014; **118(26)**, 14606-14616.

[49] S Sudewi, CH Li, S Dayalan, M Zulfajri, PV Sai Sashankh and GG Huang. Enhanced fluorescent iron oxide quantum dots for rapid and interference free recognizing lysine in dairy products. *Spectrochimica Acta Part A: Molecular and Biomolecular Spectroscopy* 2022; **279(15)**, 21453.

[50] S Pujar and GK Rao. Annealing induced strong NBE emission of SILAR deposited ZnO thin

films. *Materials Today: Proceedings* 2022; **55**, 56-61.

[51] S Arsalani, J Oliveira, EJ Guidelli, JFDF Araujo, F Wiekhorst and O Baffa. Synthesis of radioluminescent iron oxide nanoparticles functionalized by anthracene for biomedical applications. *Colloids and Surfaces A: Physicochemical and Engineering Aspects* 2020; **602**, 125105.

[52] AL Flores, N Medina-Berríos, W Pantoja-Romero, DB Plaza, K Kisslinger, J Beltran-Huarac, G Morell and BR Weiner. Geometry and surface area optimization in iron oxide nanoparticles for enhanced magnetic properties. *ACS Omega* 2024; **9(30)**, 32980-32990.

[53] A Tufani and A Qureshi. Iron oxide nanoparticles based magnetic luminescent quantum dots (MQDs) synthesis and biomedical/biological applications: A review. *Materials Science and Engineering: C* 2021, **118**, 111545.

[54] N Chekina, D Horák, P Jendelová, M Trchová, MJ Beneš, M Hrubý, V Herynek, K Turnovcová and E Syková. Fluorescent magnetic nanoparticles for biomedical applications. *Journal of Materials Chemistry* 2011; **21**, 7630-7639.

[55] X Sun, A Tayal, A Ullrich, O Petracic and S Haas. Phase composition of iron oxide nanoparticles studied using hard X-ray absorption spectroscopy. *The Journal of Physical Chemistry C* 2023; **127(25)**, 12077-12083.

[56] H Donya, TA Taha, A Alruwaili, IBI Tomsah and M Ibrahim. Micro-structure and optical spectroscopy of PVA/iron oxide polymer nanocomposites. *Journal of Materials Research and Technology* 2020; **9(4)**, 9189-9194.

[57] MY Liao, CH Wu, PS Lai, J Yu, HP Lin, TM Liu and CC Huang. Surface state mediated NIR 2-photon fluorescence of iron oxides for nonlinear optical microscopy. *AIP Advances* 2012; **23(16)**, 2044-2051.

[58] I Castellanos-Rubio, M Insausti, E Garaio, IG Muro, F Plazaola, T Rojo and L Lezama. Fe_3O_4 nanoparticles prepared by the seeded-growth route for hyperthermia: electron magnetic resonance as a key tool to evaluate size distribution in magnetic nanoparticles. *Nanoscale* 2014; **6**, 7542-7552.

[59] SW Ge, XY Wang, T Chang, B Chen, P Hu, FF Yang, Q Cao, F Yang, L Kang and KS Wang. Fe_3O_4 nanoparticles synthesized by 1-step reduction with nanoscale size-dependent magnetic properties. *Journal of Sol-Gel Science and Technology* 2023; **105**, 98-105.

[60] SA Kulkarni, PS Sawadh, PK Palei and KK Kokate. Effect of synthesis route on the structural, optical and magnetic properties of Fe_3O_4 nanoparticles. *Ceramics International* 2014; **40(1)**, 1945-1949.

[61] P Hu, S Zhang, H Wang, D Pan, J Tian, Z Tang and AA Volinsky. Heat treatment effects on Fe_3O_4 nanoparticles structure and magnetic properties prepared by carbothermal reduction. *Journal of Alloys and Compounds* 2011; **509(5)**, 2316-2319.

[62] AH Rezayan, M Mousavi, S Kheirjou, G Amoabediny, MS Ardestani and J Mohammadnejad. Monodisperse magnetite (Fe_3O_4) nanoparticles modified with water soluble polymers for the diagnosis of breast cancer by MRI method. *Journal of Magnetism and Magnetic Materials* 2016; **420**, 210-217.

[63] S Wu, A Sun, FQ Zhai, J Wang, WH Xu, Q Zhang and AA Volinsky. Fe_3O_4 magnetic nanoparticles synthesis from tailings by ultrasonic chemical co-precipitation. *Materials Letters* 2011; **65(12)**, 1882-1884.

[64] H Zhang and GQ Zhu. One-step hydrothermal synthesis of magnetic Fe_3O_4 nanoparticles immobilized on polyamide fabric. *Applied Surface Science* 2012; **258(11)**, 4952-4959.